

Article

Prediction of the Surface Roughness in Ultrasonic Vibration-Assisted Grinding of Dental Zirconia Ceramics Based on a Single-Diamond Grit Model

Xingzhi Xiao * , Gang Li and Zhihua Li

School of Mechanical Engineering, Nanjing University of Science and Technology, Nanjing 210094, China; jingganglee@outlook.com (G.L.); lzhnjst@126.com (Z.L.)

* Correspondence: xingzhi.xiao@njust.edu.cn

Abstract: Ultrasonic vibration-assisted grinding (UVAG) is regarded as a superior method for the fabrication of ceramic dentures, due to its outstanding performance in hard and brittle materials' machining. The surface roughness of dentures has a critical effect on the bonding and wear performance between dentures and natural teeth. Accomplishing the prediction of surface roughness will promote the application of UVAG in dental restoration significantly. However, the investigation about surface roughness modeling in the UVAG of ceramics is limited. In this study, a comprehensive surface roughness model was proposed with the consideration of the diamond grits' random distribution, brittle fracture removal, and ultrasonic vibration characteristics. Based on the indentation fracture removal mechanism, the material removal process was modeled. Rayleigh's probability density function was introduced to characterize the random distribution of the grits. Besides, the ultrasonic vibration was considered via the analysis of the single-diamond grit motion. Finally, the comprehensive model was developed with the consideration of all the diamond grits. Afterward, the verification experiments were carried out. The experimental results agreed well with the model predictions. Therefore, the comprehensive model can be applied to evaluate the surface roughness and can provide an in-depth understanding of the surface formation in the UVAG of ceramics.

Keywords: comprehensive model; dental ceramics; single-diamond grit; surface roughness; ultrasonic vibration-assisted grinding



Citation: Xiao, X.; Li, G.; Li, Z. Prediction of the Surface Roughness in Ultrasonic Vibration-Assisted Grinding of Dental Zirconia Ceramics Based on a Single-Diamond Grit Model. *Micromachines* **2021**, *12*, 543. <https://doi.org/10.3390/mi12050543>

Academic Editor: Chang-Hwan Choi

Received: 1 April 2021
Accepted: 7 May 2021
Published: 10 May 2021

Publisher's Note: MDPI stays neutral with regard to jurisdictional claims in published maps and institutional affiliations.



Copyright: © 2021 by the authors. Licensee MDPI, Basel, Switzerland. This article is an open access article distributed under the terms and conditions of the Creative Commons Attribution (CC BY) license (<https://creativecommons.org/licenses/by/4.0/>).

1. Introduction

Zirconia ceramics have been widely used in prosthodontics due to their superior biocompatibility, outstanding aesthetics, sufficient mechanical strength, and excellent wear resistance [1]. Meanwhile, because of their high hardness and low fracture toughness, ultrasonic vibration-assisted grinding (UVAG) technology has been introduced to fulfill the direct machining of dental ceramics [2]. As a hybrid machining method, UVAG has been proven to be an effective processing technology for hard and brittle materials [3,4]. The surface roughness of dentures (ceramic crowns, inlays, and implants) has a vital effect on oral health, wear performance, and interfacial bonding properties between dentures and natural teeth, which affects the service performance eventually [5]. Therefore, further studies, in particular for the modeling and prediction of surface roughness in the UVAG of dental ceramics, should be carried out to improve the service life of dentures.

Extensive experimental studies have been conducted on surface roughness in the UVAG of brittle materials, and the influences of machining variables (spindle rotational speed, feed rate, and cutting depth) on surface roughness have been revealed [6–8]. With the assistance of ultrasonic vibration, the surface quality is better compared to conventional grinding [9]. For dental ceramics, the machined surface roughness has a crucial effect on the service life of ceramic dentures. The outer surface roughness of the dentures plays an important role in friction and wear performances between the dentures and the natural

teeth, while the inner surface roughness of the dentures determines the adhesive properties between the dentures and the substrates [10]. Hence, realizing the prediction of surface roughness will be beneficial to obtain superior wear performances and adhesive properties. However, the current investigations for the surface roughness prediction in the UVAG of brittle materials are limited. Chen et al. [11] proposed a mathematical simulation model to predict the surface roughness in UVAG by dividing up the workpiece into a grid and calculating the minimum value of all diamond grits left at each grid point. The model was based on the plastic shear removal mechanism, which is inappropriate for brittle materials' machining. Zhang et al. [12] proposed a statistical predictive model based on the random distribution of diamond grits in the UVAG of silica glass. It was assumed that the material removed coincided with the overlapping volume between diamond grits and the workpiece, which is inconsistent with the actual material removal mode. Although several surface roughness models for traditional grinding of ceramics have been developed, the ultrasonic vibration characteristics were not included [13,14].

Diamond grits' random distribution, brittle fracture removal, and ultrasonic vibration are the three typical and important characteristics in the UVAG of brittle materials. To reveal the surface roughness formation theoretically and predict the surface roughness accurately, the effects of these three characteristics should be considered during modeling. However, the existing research in the UVAG of brittle materials did not consider all three factors at the same time. Therefore, a comprehensive model is urgently required to reveal the formation mechanism and fulfill the effective prediction of surface roughness in the UVAG of brittle materials. More specifically, the surface roughness discussed in this paper is the arithmetic mean deviation of the assessed profile (R_a). Based on the probabilistic approach of surface roughness prediction used in conventional grinding [15], a comprehensive model was proposed with the integration of the mentioned three factors. The grits random distribution was characterized by the probability density function of the chip thickness. The generation and propagation of the lateral cracks were modeled to clarify the material brittle fracture removal mechanism. Besides, with the kinematic analysis of a single-diamond grit, the ultrasonic vibration characteristics were considered. Finally, the prediction model was developed, and then, the pilot experiments were conducted to verify the model.

The paper is organized into five sections. Following this Introduction section, Section 2 models the material brittle fracture removal process. The comprehensive model for the surface roughness prediction is developed step-by-step in Section 3. In Section 4, pilot experiments are conducted to verify the developed model. Conclusions are drawn in Section 5.

2. Modeling of the Material Brittle Fracture Removal Process

Surface roughness is the representation of surface quality, which is decided by the surface formation process. Therefore, the material removal mechanism should be clarified prior to the modeling. Zirconia ceramics, as one of the typical brittle materials, have different material removal mechanisms compared with metals. According to the existing studies, two different material removal modes are discovered in ceramic machining. They are ductile removal and brittle fracture removal, respectively, which are determined by the undeformed chip thickness [16].

In this paper, only the dominating brittle fracture removal mode was considered. This method has been used and validated in other studies [17,18]. The brittle fracture removal in the grinding of ceramics is likened to the indentation fracture process, as illustrated in Figure 1a. As the diamond grit cuts the workpiece gradually, the deformation zone is formed under the diamond grit. Then, the medial crack is generated and propagates toward the inner part of the workpiece. The lateral cracks initiate and propagate as the diamond grit leaves the workpiece gradually. Finally, the material removal is formed as the lateral cracks reach the workpiece surface. The length and depth of the lateral cracks can

be calculated as Equations (1) and (2) [19]. The diamond grits were assumed to be rigid octahedrons of the same size, as shown in Figure 2.

$$C_l = C_2 \left(\cot \frac{\alpha}{2} \right)^{\frac{5}{12}} \cdot \left[\frac{E^{\frac{3}{4}}}{H_v K_{IC} (1 - v^2)^{\frac{1}{2}}} \right]^{\frac{1}{2}} \cdot F_n^{\frac{5}{8}} \quad (1)$$

$$C_h = C_2 \left(\cot \frac{\alpha}{2} \right)^{\frac{1}{3}} \cdot \frac{E^{\frac{1}{2}}}{H_v} \cdot F_n^{\frac{1}{2}} \quad (2)$$

where H_v is the hardness of the workpiece material in MPa; K_{IC} is the fracture toughness of the workpiece material in $\text{MPa} \cdot \text{m}^{1/2}$; α is the angle between two opposite edges of a diamond grit in ($\alpha = \pi/2$ rad); E is the Young's modulus of the workpiece material in MPa; v is the Poisson's ratio of the workpiece material; F_n is the load applied to the abrasive grit in N; C_2 is a dimensionless constant, which is independent of the material-indenter system, and $C_2 = 0.226$ [20].

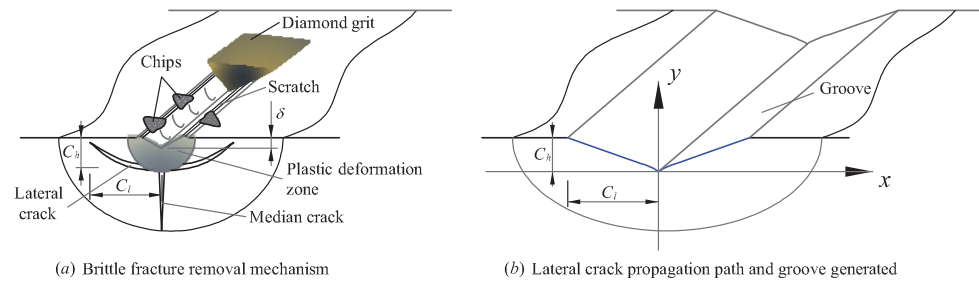


Figure 1. Brittle fracture removal mechanism and the lateral crack propagation path.

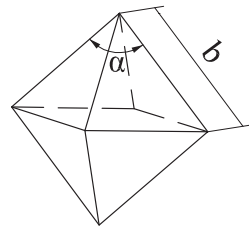


Figure 2. Illustration of the single-diamond grit.

The relationship between the load applied to the single-diamond grit F_n and the groove depth δ can be described as [20]:

$$F_n = \frac{1}{2} \zeta \delta^2 \tan^2 \frac{\alpha}{2} H_v \quad (3)$$

where ζ is the geometric factor of the indenter [19]; δ is the penetration depth of the diamond grit into the workpiece in mm. Substituting Equation (3) into Equations (1) and (2), C_l and C_h can be expressed as:

$$\begin{aligned} C_l &= C_2 \left(\cot \frac{\alpha}{2} \right)^{\frac{5}{12}} \cdot \left[\frac{E^{\frac{3}{4}}}{H_v K_{IC} (1 - v^2)^{\frac{1}{2}}} \right]^{\frac{1}{2}} \cdot \left(\frac{1}{2} \zeta \delta^2 \tan^2 \frac{\alpha}{2} H_v \right)^{\frac{5}{8}} \\ &= \left(\frac{1}{2} \right)^{\frac{5}{8}} C_2 \left(\tan \frac{\alpha}{2} \right)^{\frac{5}{8}} \zeta^{\frac{5}{8}} \frac{E^{\frac{3}{8}} H_v^{\frac{1}{8}}}{K_{IC}^{\frac{1}{4}} (1 - v^2)^{\frac{1}{4}}} \cdot \delta^{\frac{5}{4}} \\ &= C_3 \cdot \delta^{\frac{5}{4}} \end{aligned} \quad (4)$$

$$\begin{aligned}
C_h &= C_2 \left(\cot \frac{\alpha}{2} \right)^{\frac{1}{3}} \cdot \frac{E^{\frac{1}{2}}}{H_v} \cdot \left(\frac{1}{2} \xi \delta^2 \tan^2 \frac{\alpha}{2} H_v \right)^{\frac{1}{2}} \\
&= \left(\frac{1}{2} \right)^{\frac{1}{2}} C_2 \left(\tan \frac{\alpha}{2} \right)^{\frac{2}{3}} \xi^{\frac{1}{2}} \frac{E^{\frac{1}{2}}}{H_v^{\frac{1}{2}}} \cdot \delta \\
&= C_4 \cdot \delta
\end{aligned} \tag{5}$$

where $C_3 = \left(\frac{1}{2} \right)^{\frac{5}{8}} C_2 \left(\tan \frac{\alpha}{2} \right)^{\frac{5}{6}} \xi^{\frac{5}{8}} \frac{E^{\frac{3}{8}} H_v^{\frac{1}{8}}}{K_{IC}^{\frac{1}{2}} (1-v^2)^{\frac{1}{4}}}$ and $C_4 = \left(\frac{1}{2} \right)^{\frac{1}{2}} C_2 \left(\tan \frac{\alpha}{2} \right)^{\frac{2}{3}} \xi^{\frac{1}{2}} \frac{E^{\frac{1}{2}}}{H_v^{\frac{1}{2}}}$. The initiation and propagation of the lateral cracks result in the material removal when the cracks reach the workpiece surface. According to the expressions of the crack length C_l and the crack depth C_h , the mathematical relationship between C_l and C_h can be derived. This means that the crack propagation path can be expressed as a formula. Assuming that $y = C_h = C_4 \cdot \delta$, $x = C_l = C_3 \cdot \delta^{\frac{5}{4}}$, the penetration depth of the diamond grit can be easily expressed in the following two ways:

$$\delta = \frac{y}{C_4} \tag{6}$$

$$\delta = \left(\frac{x}{C_3} \right)^{\frac{4}{5}} \tag{7}$$

Equating Equation (6) to Equation (7), the expression of the crack propagation path can be obtained as:

$$y = \frac{C_4}{C_3^{\frac{4}{5}}} \cdot x^{\frac{4}{5}} \tag{8}$$

Substituting the expressions of C_3 and C_4 into Equation (8) and also considering that the value of y should be positive, the final function can be expressed as:

$$\begin{aligned}
y &= C_2^{\frac{1}{5}} \frac{E^{\frac{1}{5}} K_{IC}^{\frac{2}{5}} (1-v^2)^{\frac{1}{5}}}{H_v^{\frac{2}{5}}} \cdot x^{\frac{4}{5}} \\
&= a \cdot x^{\frac{4}{5}}
\end{aligned} \tag{9}$$

where $a = C_2^{\frac{1}{5}} \frac{E^{\frac{1}{5}} K_{IC}^{\frac{2}{5}} (1-v^2)^{\frac{1}{5}}}{H_v^{\frac{2}{5}}}$. The specific expression of the lateral crack propagation path was proposed based on the brittle fracture removal mechanism, and the shape of the crack propagation path is shown in Figure 1b. This equation was utilized as the foundation to develop the prediction model of the surface roughness in the UVAG of zirconia ceramics.

3. Development of the Prediction Model of the Surface Roughness in the UVAG of Zirconia Ceramics

UVAG might be considered as a combination of ultrasonic machining and conventional grinding [21]. The final surface formed in the UVAG of ceramics is decided by the combined cutting of numerous grits. Due to the random distribution of grits in the axial and radial directions, the penetration depth of each grit is different, and overlapping appears among the grooves. Meanwhile, the tool motion also causes the grooves to overlap. The degree of overlapping affects the final surface formation directly, so it is crucial to combine these effects in the final prediction model of the surface roughness. To get a realizable and reliable prediction model of the surface roughness, some assumptions and simplifications are needed:

1. The diamond grits were assumed to be rigid octahedrons of the same size, as shown in Figure 2. Every four adjacent triangles had a common vertex, forming a pyramid.

Only one pyramid of each octahedral particle took part in cutting; the other was buried in the metal bond.

2. The edge lengths of the single-diamond grit were assumed to be the same b .
3. For each pair of adjacent grits, the grooves generated by them only had one overlap, and the overlapping degrees for every adjacent groove were the same.

The definition of the surface roughness R_a is presented initially in Section 3.1. Then, the random distribution of the diamond grits is characterized in Section 3.2. Section 3.3 describes the derivation process of the expected value of the surface roughness $E(R_a)$. The parameter σ , which defines the probability density function, is calculated in Section 3.4. Finally, the comprehensive prediction model of the surface roughness is proposed in Section 3.5 with the consideration of the tool motion effect and tool wear.

3.1. Definition of the Surface Roughness R_a

Surface roughness is an index to characterize the surface quality quantitatively, and it is normally defined as [22]:

$$R_a = \frac{1}{l} \int_0^l |y - y_{cl}| dl \quad (10)$$

where l is the evaluation length; y_{cl} is the position of the center line so that the areas above and below the line are equal.

The statistical expression of R_a can be described as [22]:

$$R_a = \frac{1}{l} \int_{y_{min}}^{y_{max}} |y - y_{cl}| p(y) dy \quad (11)$$

where y_{max} and y_{min} are the highest and lowest peak height of the surface profile; $p(y)$ is the probability to get a peak of height y .

3.2. Grits' Random Distribution on the Tool Used in the UVAG of Ceramics

For grinding tools used in the UVAG of ceramics, the diamond grits are sintered randomly on the lateral and end faces of the metal shank, as illustrated in Figure 3a,b. The trajectory of a diamond grit in UVAG is shown in Figure 4. The motion of the diamond grit consists of the spindle rotation, spindle ultrasonic vibration, and horizontal feed motion of the tool. During the UVAG of zirconia ceramics, the diamond grits on the end face take part in cutting, and the random distribution in the axial direction results in different penetration depths for each grit. This means that the undeformed chip thickness or penetration depth of the grits is not fixed, although the cutting depth of the tool is set as constant. This is a typical characteristic in the UVAG of ceramics, and it should be considered in the comprehensive surface roughness model. Thereby, Rayleigh's probability density function proposed by Younis and Alaw [23] was introduced to describe the penetration depth δ as follows:

$$f(\delta) = \begin{cases} \left(\frac{\delta}{\sigma^2}\right) e^{-\frac{\delta^2}{2\sigma^2}} & \delta \geq 0 \\ 0 & \delta < 0 \end{cases} \quad (12)$$

where σ is a parameter that defines the probability density function completely and depends on the machining conditions.

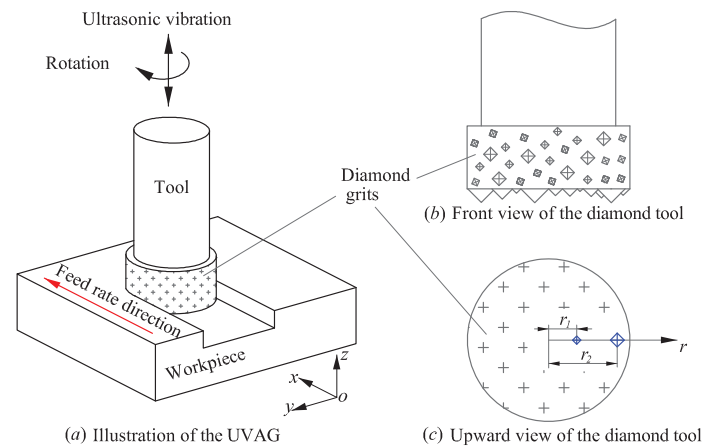


Figure 3. Random distribution of the grits on the UVAG tool.

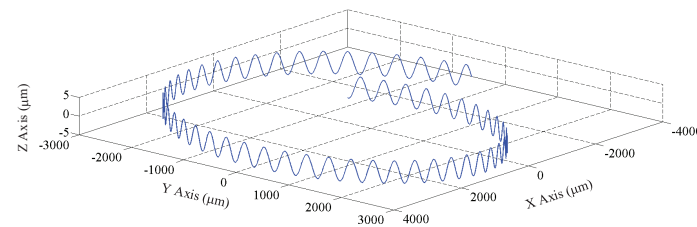


Figure 4. Trajectory of a diamond grit in UVAG.

The expected value and the standard deviation of the penetration depth δ can be expressed as:

$$E(\delta) = \sqrt{\frac{\pi}{2}} \cdot \delta \quad (13)$$

$$sd(\delta) = \sqrt{\frac{4 - \pi}{2}} \cdot \delta \quad (14)$$

Besides the random distribution in the axial direction, the diamond grits are also distributed irregularly in the radial direction. This leads to the overlapping of grooves in the radial direction, which affects the surface formation subsequently. As shown in Figure 3c, from the bottom view of the ultrasonic tool, the diamond grits are randomly positioned on the end face of the tool, while they can be generally considered as uniformly distributed on the tool end face. In that case, the diamond grits are also distributed uniformly in the radial direction of the end face. Coordinate r is the position of the grits in the radial direction, so the probability density function of r is given by:

$$f(r) = \frac{1}{R} \quad 0 < r < R \quad (15)$$

where R is the radius of the tool in mm.

The groove overlapping is mainly caused by the grit random distribution and the tool motion. In this subsection, the effect of the grit random distribution was analyzed first. From the section view of the grooves in Figure 5, two successive grooves produced by adjacent grits are illustrated. The center distance ∇w of these two grooves is introduced to characterize the overlapping.

$$\nabla w = |r_{i+1} - r_i| \quad (16)$$

where i denotes the i -th groove.

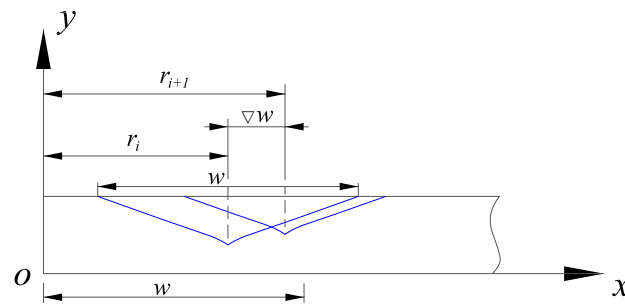


Figure 5. Section view of two adjacent grooves.

Let $w_1 = r_{i+1} - r_i$ and $w_2 = r_i$, so the expressions of r_i and r_{i+1} can be written as:

$$r_i = w_2 \quad \text{and} \quad r_{i+1} = w_1 + w_2 \quad (17)$$

To calculate the expected value of ∇w , a joint probability density function is required, which can be expressed as [15]:

$$f(w_1, w_2) = f(r_1(w_1, w_2), r_2(w_1, w_2)) |J| \quad (18)$$

where J is the Jacobian determinant [15].

Based on Equation (15), the probability density function of w_1 for the section length w is defined by the following two equations:

$$f(w_1) = \int_{w_1}^w f(w_1, w_2) dw_2 \quad w_1 > 0 \quad (19)$$

$$f'(w_1) = \int_{-w_1}^w f(w_1, w_2) dw_2 \quad w_1 < 0 \quad (20)$$

As defined in Equation (16), the center-to-center distance of two adjacent grooves ∇w is equal to w_1 . Therefore, the probability density function of the distance ∇w is equal to the combination of the probability density function of w_1 in positive and negative conditions, which can be written as:

$$f(\nabla w) = f(w_1) + f'(w_1) \quad (21)$$

According to the above probability density function, the expected value of the center-to-center distance for successive grooves in the radial direction $E(\nabla w)$ can be derived as:

$$E(\nabla w) = \int_0^w \nabla w \cdot f(\nabla w) d\nabla w = \frac{1}{3}w \quad (22)$$

The view of non-overlapping and overlapping grooves can be illustrated in Figure 6a,b, respectively. The center lines of non-overlapping and overlapping grooves y_{cl1} and y_{cl2} can be calculated according to the definition of the center line described in Equation (10). Then, the overlapping factor can be derived with the comparison of the non-overlapping and overlapping groove sections.

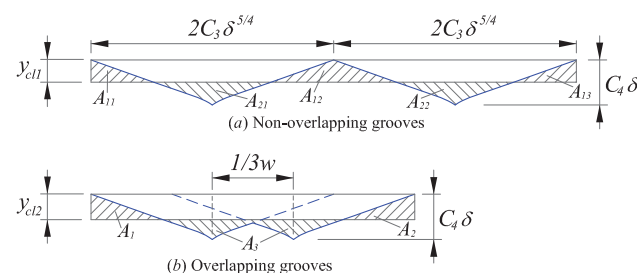


Figure 6. Illustration of non-overlapping and overlapping for two adjacent grooves.

According to the definition of y_{cl1} , the areas above and below the center line are equal, which can be expressed as:

$$A_{11} + A_{12} + A_{13} = A_{21} + A_{22} \quad (23)$$

specified as:

$$4 \left(C_3 y_{cl1} \cdot \delta^{\frac{5}{4}} - \left(C_5 \cdot \delta^{\frac{9}{4}} - \left((C_4 \delta - y_{cl1}) \left(\frac{C_4 \delta - y_{cl1}}{a} \right)^{\frac{5}{4}} - \frac{5}{9} a \left(\frac{C_4 \delta - y_{cl1}}{a} \right)^{\frac{9}{4}} \right) \right) \right) \quad (24)$$

$$= 2 \left(C_3 y_{cl1} \cdot \delta^{\frac{5}{4}} - \left(C_3 C_4 - \frac{5}{9} a C_3^{\frac{9}{5}} \right) \cdot \delta^{\frac{9}{4}} \right)$$

and simplified as:

$$y_{cl1} = \frac{C_5}{C_3} \cdot \delta \quad (25)$$

where the areas A_{11} , A_{12} , A_{13} , A_{21} , and A_{22} are illustrated in Figure 6a and $C_5 = C_3 C_4 - \frac{5}{9} a C_3^{9/5}$.

A similar method is used to get y_{cl2} .

$$y_{cl2} = C_4 \delta - \frac{5}{12} \left[\left(\frac{1}{3} \right)^{\frac{9}{5}} + 1 \right] a C_3^{\frac{4}{5}} \delta \quad (26)$$

As shown in Figure 6, the overlapping degree of the areas above and below the center line was assumed to be constant. In this case, the area above the center line was chosen to calculate the overlapping factor k_1 , which is the ratio of the area with overlapping to the area without overlapping. The specific expression of k_1 is described as:

$$lk_1 = \frac{A_1 + A_2}{A_{11} + A_{12} + A_{13}} \quad (27)$$

$$= \frac{C_3 y_{cl2} \cdot \delta^{\frac{5}{4}} - C_5 \cdot \delta^{\frac{9}{4}} + \frac{1}{a^{\frac{5}{4}}} (C_4 \delta - y_{cl2})^{\frac{9}{4}} - \frac{5}{9 a^{\frac{5}{4}}} (C_4 \delta - y_{cl2})^{\frac{9}{4}}}{2 \left(C_3 y_{cl1} \cdot \delta^{\frac{5}{4}} - C_5 \cdot \delta^{\frac{9}{4}} + \frac{1}{a^{\frac{5}{4}}} (C_4 \delta - y_{cl1})^{\frac{9}{4}} - \frac{5}{9 a^{\frac{5}{4}}} (C_4 \delta - y_{cl1})^{\frac{9}{4}} \right)}$$

Substituting Equations (25) and (26) into Equation (27), the value of k_1 can be obtained:

$$k_1 = 0.5914 \quad (28)$$

3.3. Expected Value of the Surface Roughness $E(R_a)$

As shown in Figure 7, two types of grooves are generated during the UVAG of ceramics, which depend on the relative position between the depth of the radial crack C_h and the center line y_{cl} . In this section, the center line y_{cl} was calculated to deduce the expected value of the surface roughness $E(R_a)$.

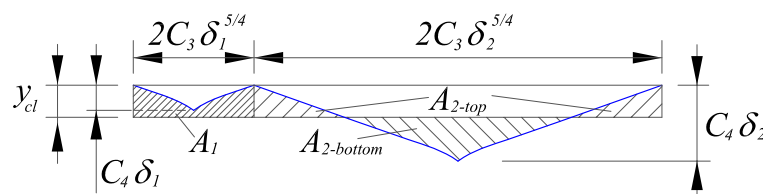


Figure 7. Profile of the grooves generated in the UVAG of ceramics.

$$p_1 E(A_1) + p_2 E(A_{2-top}) = p_2 E(A_{2-bottom}) \quad (29)$$

where p_1 and p_2 are the probabilities of a groove depth to be below or above the center line, respectively.

The specific expression of p_1 and p_2 can be derived from the probability density function of the penetration depth $f(\delta)$, which can be expressed as:

$$p_1 = \int_0^{y_{cl}} f(\delta) d\delta \quad (30)$$

$$p_2 = \int_{y_{cl}}^{\infty} f(\delta) d\delta \quad (31)$$

Considering the overlapping, the expected value of the area above the center line $E(A_1)$, in the case that the groove depth δ_1 is less than y_{cl} , can be expressed as:

$$\begin{aligned} E(A_1) &= k_1 \cdot 2E \left(C_{l-\delta_1} \cdot C_{h-\delta_1} - \int_0^{C_{l-\delta_1}} ax^{\frac{4}{5}} \cdot dx \right) \\ &= k_1 \cdot 2E \left(C_3 y_{cl} \cdot \delta_1^{\frac{5}{4}} - \left(C_3 C_4 - \frac{5}{9} a C_3^{\frac{9}{5}} \right) \cdot \delta_1^{\frac{9}{4}} \right) \\ &= k_1 \cdot 2 \left(C_3 y_{cl} \cdot E \left(\delta_1^{\frac{5}{4}} \right) - C_5 \cdot E \left(\delta_1^{\frac{9}{4}} \right) \right) \end{aligned} \quad (32)$$

In the case of a groove depth δ_1 larger than y_{cl} , the expected value of the area above the center line $E(A_{2-top})$ and the expected value of the area below the center line $A_{2-bottom}$ can be described respectively as:

$$\begin{aligned} E(A_{2-top}) &= k_1 \cdot 2E \left(C_3 y_{cl} \cdot \delta_2^{\frac{5}{4}} - \left(C_5 \cdot \delta_2^{\frac{9}{4}} - \left((C_4 \delta_2 - y_{cl}) \left(\frac{C_4 \delta_2 - y_{cl}}{a} \right)^{\frac{5}{4}} \right. \right. \right. \\ &\quad \left. \left. \left. - \frac{5}{9} a \left(\frac{C_4 \delta_2 - y_{cl}}{a} \right)^{\frac{9}{4}} \right) \right) \right) \\ &= k_1 \cdot 2 \left(C_3 y_{cl} \cdot E \left(\delta_2^{\frac{5}{4}} \right) - C_5 \cdot E \left(\delta_2^{\frac{9}{4}} \right) + \frac{4}{9} \cdot \frac{C_4^{\frac{9}{4}}}{a^{\frac{5}{4}}} \cdot E \left(\delta_2^{\frac{9}{4}} \right) \right. \\ &\quad \left. - \frac{C_4^{\frac{5}{4}}}{a^{\frac{5}{4}}} y_{cl} \cdot E \left(\delta_2^{\frac{5}{4}} \right) + \frac{5}{8} \frac{C_4^{\frac{1}{4}}}{a^{\frac{5}{4}}} y_{cl}^2 \cdot E \left(\delta_2^{\frac{1}{4}} \right) \right) \end{aligned} \quad (33)$$

$$\begin{aligned} E(A_{2-bottom}) &= k_1 \cdot 2E \left((C_4 \delta_2 - y_{cl}) \left(\frac{C_4 \delta_2 - y_{cl}}{a} \right)^{\frac{5}{4}} - \frac{5}{9} a \left(\frac{C_4 \delta_2 - y_{cl}}{a} \right)^{\frac{9}{4}} \right) \\ &= k_1 \cdot 2 \left(\frac{4}{9} \frac{C_4^{\frac{9}{4}}}{a^{\frac{5}{4}}} \cdot E \left(\delta_2^{\frac{9}{4}} \right) - \frac{C_4^{\frac{5}{4}}}{a^{\frac{5}{4}}} y_{cl} \cdot E \left(\delta_2^{\frac{5}{4}} \right) + \frac{5}{8} \frac{C_4^{\frac{1}{4}}}{a^{\frac{5}{4}}} y_{cl}^2 \cdot E \left(\delta_2^{\frac{1}{4}} \right) \right) \end{aligned} \quad (34)$$

The calculation of the expected values above requires the definition of the probability density functions for those cases where the chip thickness is below and above the center line. Therefore, two new probability density functions must be defined in each region as:

$$f_1(\delta) = \frac{f(\delta)}{\int_0^{y_{cl}} f(\delta) d\delta} \quad 0 \leq \delta < y_{cl} \quad (35)$$

$$f_2(\delta) = \frac{f(\delta)}{\int_{y_{cl}}^{\infty} f(\delta) d\delta} \quad y_{cl} \leq \delta < \infty \quad (36)$$

Substituting Equations (30)–(36) into Equation (29), the expression of the center line y_{cl} can be deduced:

$$C_3 y_{cl} \left(p_1 E \left(\delta_1^{\frac{5}{4}} \right) + p_2 E \left(\delta_2^{\frac{5}{4}} \right) \right) = C_5 \left(p_1 E \left(\delta_1^{\frac{9}{4}} \right) + p_2 E \left(\delta_2^{\frac{9}{4}} \right) \right) \quad (37)$$

and simplified as:

$$y_{cl} = \frac{C_5}{C_3} \cdot E(\delta) \quad (38)$$

Combining the area above and below the center line, the expected value for the surface roughness can be expressed as:

$$E(R_a) = p_1 E(R_{a1}) + p_2 E(R_{a2}) \quad (39)$$

where $E(R_{a1})$ and $E(R_{a2})$ are the expected values of the surface roughness for a groove depth δ below and above the center line.

The expected value of the surface roughness contribution of the grooves' depths below the center line $E(R_{a1})$ can be calculated by:

$$\begin{aligned} E(R_{a1}) &= E \left(\frac{A_1}{2C_3 \delta_1^{\frac{5}{4}}} \right) \\ &= k_1 \cdot \left(y_{cl} - \frac{C_5}{C_3} \cdot E(\delta_1) \right) \end{aligned} \quad (40)$$

The expected value of the surface roughness contribution of the grooves' depths above the center line $E(R_{a2})$ can be described by:

$$\begin{aligned} E(R_{a2}) &= E \left(\frac{A_{2-top} + A_{2-bottom}}{2C_3 \delta_2^{\frac{5}{4}}} \right) \\ &= k_1 \cdot \left(y_{cl} - \frac{C_5}{C_3} \cdot E(\delta_2) + \frac{8}{9} \cdot \frac{C_4^{\frac{9}{4}}}{C_3 a^{\frac{5}{4}}} \cdot E(\delta_2) \right. \\ &\quad \left. - 2 \cdot \frac{C_4^{\frac{5}{4}}}{C_3 a^{\frac{5}{4}}} y_{cl} + \frac{5}{4} \cdot \frac{C_4^{\frac{1}{4}}}{C_3 a^{\frac{5}{4}}} y_{cl}^2 \cdot E \left(\frac{1}{\delta_2} \right) \right) \end{aligned} \quad (41)$$

The probabilities of the lateral crack depth to be below and above the center line are as follows:

$$p_1 = \int_0^{y_{cl}} f(\delta) d\delta = 1 - e^{-\frac{y_{cl}^2}{2\sigma^2}} \quad (42)$$

The probability of the lateral crack depth above the center line is calculated as:

$$p_2 = \int_{y_{cl}}^{\infty} f(\delta) d\delta = 1 - p_1 = e^{-\frac{y_{cl}^2}{2\sigma^2}} \quad (43)$$

Substituting Equations (40)–(43) into Equation (39), the expected value of $E(R_a)$ can be obtained:

$$E(R_a) = 0.3635 k_1 \cdot \sigma \quad (44)$$

3.4. Calculation of the Parameter σ

Based on Equation (44), the parameter σ needs to be obtained to get the expected value of surface roughness $E(R_a)$.

With the consideration of the interference between adjacent diamond grits, the schematic illustration of the theoretical volume removed (polyhedron $abcd - e f g h$) can be seen in Figure 8. From the figure, the expected volume removed by a single-diamond grit can be defined as:

$$E(V_s) = \left(C_5 \cdot E\left(\delta^{\frac{9}{4}}\right) + \frac{1}{3} C_3 C_4 \cdot E\left(\delta^{\frac{9}{4}}\right) - \frac{5}{9} \left(\frac{1}{3}\right)^{\frac{5}{9}} a C_3^{\frac{9}{5}} \cdot E\left(\delta^{\frac{9}{4}}\right) \right) \cdot \frac{2\pi n R}{60} \cdot \frac{E(\delta)}{2A f_v} \quad (45)$$

where n is the spindle rotational speed in min^{-1} ; A is the ultrasonic vibration amplitude in μm ; f_v is the ultrasonic vibration frequency in Hz.

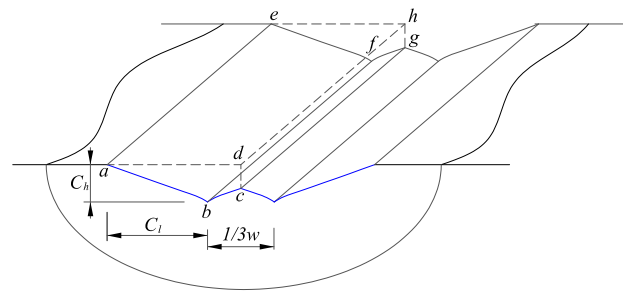


Figure 8. Illustration of the theoretical material removal volume of a single-diamond grit.

According to the machining parameters, the actual volume removed during UVAG can be obtained as:

$$V_a = 2R(a_p + A)v_f \frac{1}{f_v} \quad (46)$$

where v_f is the feed rate in mm/min ; a_p denotes the cutting depth in mm .

The volume removed obtained from theoretical analysis should be equal to the volume removed calculated using the machining parameters. Therefore, equating the theoretical volume removed with combining the diamond grit number to the actual volume removed is described as:

$$N_a \cdot E(V_s) = V_a$$

$$N_a \cdot \left(C_5 + \frac{1}{3} C_3 C_4 - \frac{5}{9} \left(\frac{1}{3}\right)^{\frac{5}{9}} a C_3^{\frac{9}{5}} \right) \cdot E\left(\delta^{\frac{13}{4}}\right) \cdot \frac{2\pi n R}{60} \cdot \frac{1}{2A f_v} = 2R(a_p + A)v_f \frac{1}{f_v} \quad (47)$$

Thus, the expected value of the penetration depth can be obtained:

$$E\left(\delta^{\frac{13}{4}}\right) = \frac{120(a_p + A)v_f A}{\pi n \cdot N_a \cdot \left(C_5 + \frac{1}{3} C_3 C_4 - \frac{5}{9} \left(\frac{1}{3}\right)^{\frac{5}{9}} a C_3^{\frac{9}{5}} \right)} \quad (48)$$

where $E\left(\delta^{\frac{13}{4}}\right) = \int_0^\infty \frac{\delta^{\frac{17}{4}}}{\sigma^2} e^{-\frac{\delta^2}{2\sigma^2}} d\delta = 4.4938\sigma^{\frac{13}{4}}$.

Therefore, σ can be derived from Equation (48) with the following expression:

$$\sigma = \left(\frac{80(a_p + A)v_f A}{3\pi n \cdot N_a \cdot \left(C_5 + \frac{1}{3} C_3 C_4 - \frac{5}{9} \left(\frac{1}{3}\right)^{\frac{5}{9}} a C_3^{\frac{9}{5}} \right)} \right)^{\frac{4}{13}} \quad (49)$$

3.5. Comprehensive Predictive Model for the Surface Roughness

As mentioned above, the tool motion also affects the grooves overlapping and, subsequently, the surface roughness. The tool motion was determined by the cutting parameters

(spindle rotational speed n , feed rate v_f , and cutting depth a_p). Besides, the tool wear was not considered in the above modeling process, which is mainly affected by the machining time t . In this case, a parameter $k_2 = f(n, v_f, a_p, t)$ was introduced to characterize the influence of the tool motion on the grooves overlapping and tool wear. Therefore, the final comprehensive surface roughness model can be described as:

$$E(R_a) = k_2 \cdot 0.3635k_1\sigma \quad (50)$$

Substituting Equations (28) and (49) and the expression of k_2 into Equation (50), the comprehensive surface model can be rewritten as:

$$\begin{aligned} E(R_a) &= 0.3635 \times 0.5914 \cdot f(n, v_f, a_p, t) \cdot \left(\frac{80(a_p + A)v_f A}{3\pi n \cdot N_a \cdot \left(C_5 + \frac{1}{3}C_3C_4 - \frac{5}{9}\left(\frac{1}{3}\right)^{\frac{9}{5}} a C_3^{\frac{9}{5}} \right)} \right)^{\frac{4}{13}} \\ &= 0.2150 \cdot f(n, v_f, a_p, t) \cdot \left(\frac{80(a_p + A)v_f A}{3\pi n \cdot N_a \cdot \left(C_5 + \frac{1}{3}C_3C_4 - \frac{5}{9}\left(\frac{1}{3}\right)^{\frac{9}{5}} a C_3^{\frac{9}{5}} \right)} \right)^{\frac{4}{13}} \end{aligned} \quad (51)$$

The number of diamond grits N_a can be obtained as [15]:

$$\begin{aligned} N_a &= \left[\frac{0.88 \times 10^{-3}}{\frac{\sqrt{2}}{3}b^3\rho} \cdot \frac{C_a}{100} \right]^{\frac{2}{3}} \cdot \pi R^2 \\ &= C_0 \cdot \frac{C_a^{\frac{2}{3}}}{b^2} \cdot \pi R^2 \end{aligned} \quad (52)$$

where C_a is the diamond grits concentration [17]; ρ is the density of the abrasive material in g/mm^3 , $\rho = 3.25 \times 10^{-3} \text{ g}/\text{mm}^3$; C_0 is a dimensionless constant, $C_0 = [3 \times 0.88 \times 10^{-3} / (100 \times 2^{0.5}\rho)]^{\frac{2}{3}} = 0.033$.

4. Experimental Verification

4.1. Experimental Setup

As illustrated in Figure 9, the slots were machined with the UVAG method. The machining center (DMG Ultrasonic 20 linear, DMG, Berlin, Germany) mainly consisted of an ultrasonic spindle system, a numerical control machining system, and a coolant system.

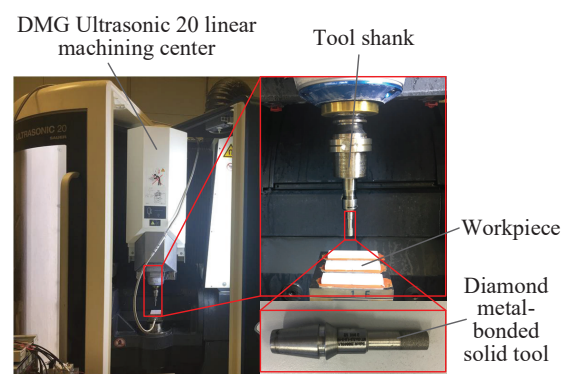


Figure 9. Experimental setup adopted for the UVAG experiments.

The maximum spindle rotational speed with ultrasonic vibration was $10,000 \text{ min}^{-1}$, while the maximum spindle rotational speed without ultrasonic vibration was $42,000 \text{ min}^{-1}$. The vibration frequency varied from 20 kHz to 50 kHz for the different tool-workpiece systems adopted. The vibration amplitude was measured by a laser vibrometer (Polytec OFV

353 sensor head and OFV 2200 vibrometer controller). The tool used in the experiments was provided by Schott Diamantwerkzeuge GmbH in Germany, and it was a diamond metal-bonded solid tool with a diameter of 6 mm and a diamond grit size of D91. The Taylor Hobson profilometer was used to measure the surface roughness of the slots, as illustrated in Figure 10. The measurement direction was the same as the feed rate direction. Each slot was measured six times, and the arithmetic average value was obtained as the global surface roughness of the slot. The cut-off was 0.8 mm; the measurement length was 8 mm; and the spacing was 0.8 mm.



Figure 10. Measurement method adopted after the UVAG experiments.

4.2. Design of Experiments

The workpiece materials were zirconia ceramics provided by Qinhuangdao Aidite High-Technical Ceramics, CO., Ltd (Qinhuangdao, China). The compositions and the primary mechanical properties of the zirconia ceramics are shown in Tables 1 and 2, respectively. The dimensions of the zirconia ceramics were $30 \times 15 \times 5$ mm.

Table 1. Compositions of the dental zirconia ceramics used for the experiments.

| Composition | ZrO ₂ | Y ₂ O ₃ | Al ₂ O ₃ | SiO ₂ | Fe ₂ O ₃ | Na ₂ O |
|-------------|------------------|-------------------------------|--------------------------------|------------------|--------------------------------|-------------------|
| Content (%) | <96 | 5.30 | 0.25 | ≤0.002 | ≤0.002 | ≤0.002 |

Table 2. Properties of the dental zirconia ceramics used for the experiments.

| Property | Unit | Value |
|------------------------------|----------------------|----------|
| Bending strength | MPa | 800–1000 |
| Fracture strength | MPa | 1200 |
| Fracture toughness, K_{IC} | MPa·m ^{1/2} | 6 |
| Vickers hardness, H_v | GPa | 12 |
| Young's modulus, E | GPa | 210 |
| Density, ρ | g/cm ³ | 6.05 |

Twenty-four groups of experiments were carried out. Considering the effect of the tool wear, the odd-group experiments were selected to calibrate k_2 , and all 24 experiments were used to verify the proposed model. The details of the experimental design are shown in Table 3. There were three input variables (n , v_f , and a_p). Each of these 3 parameters assumed 8 different values, which explained why 24 experiments were performed. Other variables, such as the ultrasonic vibration frequency and ultrasonic vibration amplitude, were kept constant with a value of 25,010 Hz and 5 μ m, respectively.

Table 3. Details of the experimental design.

| Series No. | n (min ⁻¹) | v_f (mm/min) | a_p (μm) | Experimental R_a (μm) | Predicted R_a (μm) |
|------------|--------------------------|----------------|------------|-------------------------|----------------------|
| 1 | 2000 | 30 | 6 | 0.4954 | 0.4941 |
| 2 | 3500 | 30 | 6 | 0.2205 | 0.3825 |
| 3 | 5000 | 30 | 6 | 0.3223 | 0.3224 |
| 4 | 6500 | 30 | 6 | 0.3573 | 0.3228 |
| 5 | 4500 | 5 | 6 | 0.4647 | 0.4654 |
| 6 | 4500 | 20 | 6 | 0.6368 | 0.5151 |
| 7 | 4500 | 35 | 6 | 0.5938 | 0.5867 |
| 8 | 4500 | 50 | 6 | 0.5607 | 0.4629 |
| 9 | 4500 | 30 | 5 | 0.6221 | 0.6301 |
| 10 | 4500 | 30 | 8 | 0.6828 | 0.6913 |
| 11 | 4500 | 30 | 11 | 0.8129 | 0.8187 |
| 12 | 4500 | 30 | 14 | 0.9806 | 0.9459 |
| 13 | 2500 | 30 | 6 | 0.7825 | 0.7782 |
| 14 | 4000 | 30 | 6 | 0.7648 | 0.7015 |
| 15 | 5500 | 30 | 6 | 0.6698 | 0.6625 |
| 16 | 7000 | 30 | 6 | 0.6457 | 0.6296 |
| 17 | 4500 | 10 | 6 | 0.6120 | 0.6103 |
| 18 | 4500 | 25 | 6 | 0.6509 | 0.7595 |
| 19 | 4500 | 40 | 6 | 0.4713 | 0.4710 |
| 20 | 4500 | 55 | 6 | 0.5049 | 0.4333 |
| 21 | 4500 | 30 | 7 | 0.5404 | 0.5533 |
| 22 | 4500 | 30 | 10 | 0.5259 | 0.5483 |
| 23 | 4500 | 30 | 13 | 0.6109 | 0.6043 |
| 24 | 4500 | 30 | 15 | 0.6829 | 0.6674 |

4.3. Obtaining k_2 and Surface Roughness Prediction

k_2 contains the effect of the tool motion on the grooves overlapping and tool wear. The tool wear was not linear with time: initially, it increased sharply, then it remained stable, and finally, it rose rapidly again. Therefore, using the linear estimation or least squares estimation to calibrate k_2 was not effective. In this case, the backpropagation neural network algorithm was chosen to get the function $f(n, v_f, a_p, t)$. A typical backpropagation neural network usually consists of an input layer, a hidden layer, and an output layer. According to the expression of k_2 , the number of neurons of the input layer was selected as 4. The number of hidden layers was 1, and the number of neurons was 5. The number of output neurons was 1, and the structure of the backpropagation neural network is shown in Figure 11. Before inputting the training sample, the experimental data needed to be normalized, and the data of each parameter was normalized to the interval (0, 1). The training program was written in MATLAB, and the momentum gradient descent method was used to train the established neural network model. The minimum error of the training target was 0.0005, and the maximum allowed training step size was 200,000 steps. The training model was used to train 12 sets of odd-group experimental data. When the training error was less than the minimum error of the training target, the training ended, and a backpropagation neural network prediction model for k_2 was formed. Then, the comprehensive predictive model for the surface roughness could be obtained. The comparison between the experimental results and the prediction results is shown in Figure 12.

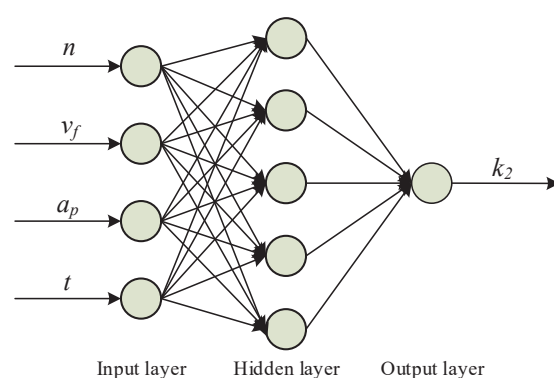


Figure 11. Structure of the implemented backpropagation neural network.

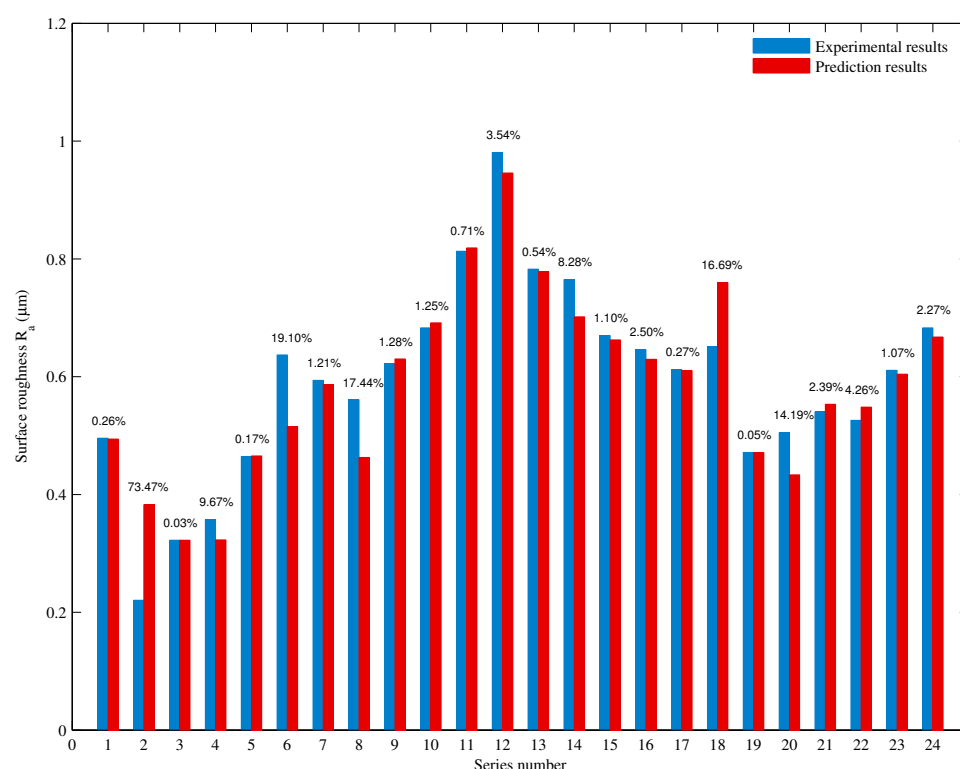


Figure 12. Comparison analysis between prediction and experimental results.

As shown in Figure 12, the predictive results agreed well with the experimental ones, and the total average relative error was 7.57%, which means that the proposed model can be used for surface roughness prediction. For the relative error of each individual experiment, the maximum value was 73.47% in the second experiment. This could be caused by the micro-breakage of the sharp cutting edges. A new diamond tool was used for the first 12 groups of experiments, and another new tool was used for the last 12 groups of experiments. The cutting edges of the grits were sharp in the initial process. These sharp edges were apt to break with the assistance of vibration, and in this way, numerous micro edges were formed. These micro edges improved the surface quality distinctively, which resulted in an evident decrease of the surface roughness value (from 0.4954 μm in the first experiment to 0.2205 μm in the second experiment). The micro-breakage phenomenon was also mentioned in Ding et al. [24]. Therefore, the abrupt change of the surface roughness value in the second experiment led to a large deviation between the prediction and experimental results. If the second experiment were removed from the verification, the total average relative error could be 4.71%, which indicated a high prediction accuracy of the proposed model.

The effects of the input variables on the surface roughness are illustrated in Figure 13. From the experimental results, the surface roughness showed a downward trend as the spindle rotational speed increased, while it showed a reverse trend as the cutting depth increased. With increasing feed rate, the surface roughness showed a fluctuating growth trend. Similar effects can also be found in the prediction results, which further validate the proposed model. Similar results were also obtained in previous studies [2,8].

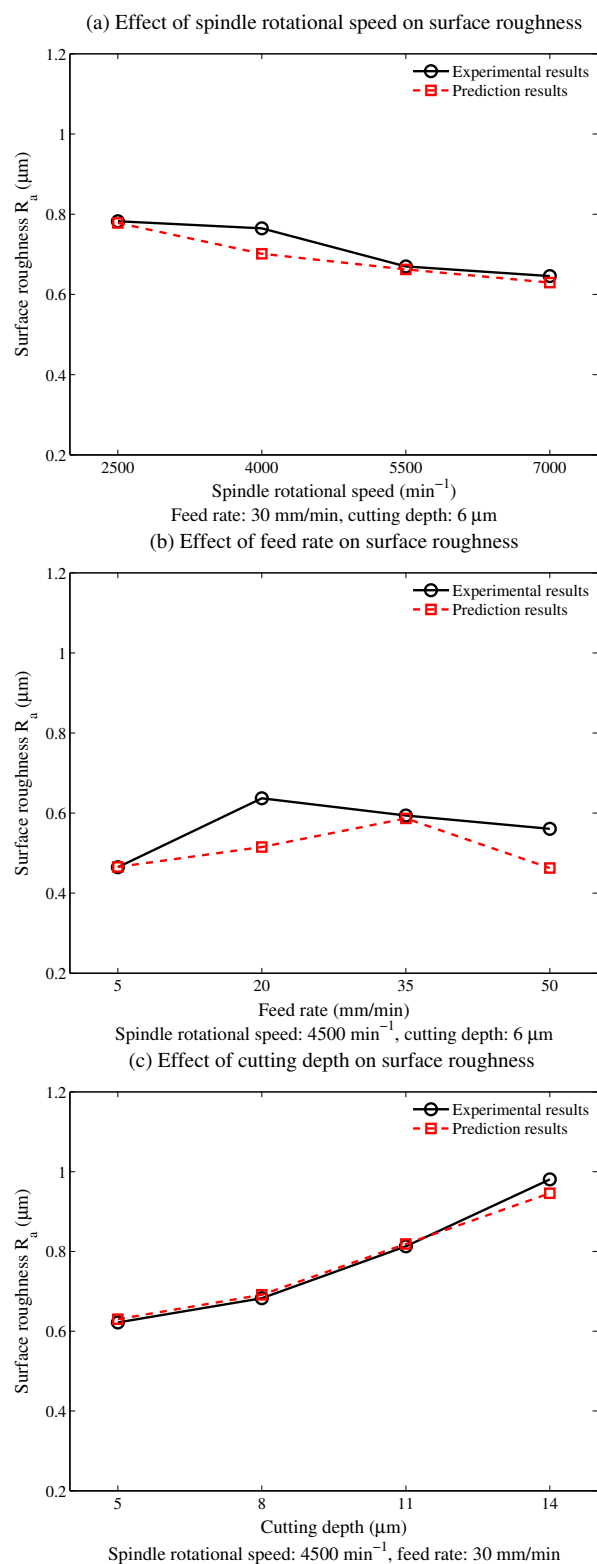


Figure 13. Effects of the input variables on the surface roughness.

5. Conclusions

In this paper, the mathematical expression of the lateral crack propagation path was derived firstly. Afterward, Rayleigh's probability density function was introduced to describe the penetration depth of the diamond grits. Finally, with the consideration of the ultrasonic vibration characteristics, a comprehensive predictive model for the surface roughness in UVAG of ceramics was proposed. The relationship between input variables and the surface roughness was analyzed both theoretically and experimentally. The following conclusions can be summarized from the study:

1. The prediction results were very consistent with the experimental ones, and the total average relative error was 7.57%. These results verified the validity of the proposed model. Therefore, the proposed model can be applied for surface roughness prediction in the UVAG of ceramics.
2. The effects of the diamond grits' random distribution, brittle fracture removal, and ultrasonic vibration on the surface roughness were considered during the modeling process. This provided an in-depth understanding of the formation of surface roughness in the UVAG of ceramics and can be also considered as the basis for future parameter optimization.
3. From the developed model, the surface roughness decreased with the rise of the spindle rotational speed, while it showed the opposite trend with increasing cutting depth. Besides, the surface roughness had a fluctuating growth trend with increasing feed rate. Similar results were also obtained in previous studies [2,8].

To further improve the accuracy of the proposed model, reverse engineering methods could be used to obtain the real distribution and shape of the diamond grits. For example, a scanner can be utilized to get the 3D data of the diamond grits, and the distribution characteristics can be derived from statistical analysis.

Author Contributions: Conceptualization, X.X.; methodology, X.X.; validation, X.X.; formal analysis, X.X.; investigation, X.X.; resources, X.X. and Z.L.; writing—original draft preparation, X.X.; writing—review and editing, G.L.; funding acquisition, X.X. All authors have read and agreed to the published version of the manuscript.

Funding: This research was funded by the National Natural Science Foundation of China (Grant No. 51675284).

Acknowledgments: The authors appreciate the financial support of the National Natural Science Foundation of China (Grant No. 51675284) and the hardware support from the Micro and Precision Engineering research group at KU Leuven.

Conflicts of Interest: The authors declare no conflict of interest.

Abbreviations

| | |
|----------|---|
| UVAG | Ultrasonic vibration-assisted grinding |
| A | Ultrasonic vibration amplitude |
| a_p | Cutting depth |
| b | Edge length of a single-diamond grit |
| C_a | Diamond grit concentration |
| C_h | Crack depth |
| C_l | Crack length |
| E | Young's modulus of the workpiece material |
| $E(R_a)$ | Expected value of surface roughness |
| F_n | Load applied to the abrasive grit |
| f_v | Ultrasonic vibration frequency |

| | |
|----------|---|
| H_v | Hardness of the workpiece material |
| l | Evaluation length |
| n | Spindle rotational speed |
| N_a | Number of diamond grits |
| r | Position of the grits in the radial direction |
| R | Radius of the tool |
| R_a | Surface roughness (arithmetic mean deviation of the assessed profile) |
| ν | Poisson's ratio of the workpiece material |
| v_f | Feed rate |
| y | Crack propagation path |
| α | Angle between two opposite edges of a diamond grit |
| δ | Penetration depth of a diamond grit into the workpiece |
| ξ | Geometric factor of the indenter |
| ρ | Density of the abrasive material |
| σ | Probability density function parameter |

References

- Manicone, P.F.; Iommetti, P.R.; Raffaelli, L. An overview of zirconia ceramics: Basic properties and clinical applications. *J. Dent.* **2007**, *35*, 819–826. [\[CrossRef\]](#)
- Churi, N.J.; Pei, Z.J.; Shorter, D.C.; Treadwell, C. Rotary ultrasonic machining of dental ceramics. *J. Mach. Mach. Mater.* **2009**, *6*, 270–284. [\[CrossRef\]](#)
- Lv, D.; Huang, Y.; Wang, H.; Tang, Y.; Wu, X. Improvement effects of vibration on cutting force in rotary ultrasonic machining of BK7 glass. *J. Mater. Process. Technol.* **2013**, *213*, 1548–1557. [\[CrossRef\]](#)
- Tesfay, H.D.; Xu, Z.; Li, Z.C. Ultrasonic vibration assisted grinding of bio-ceramic materials: An experimental study on edge chippings with Hertzian indentation tests. *Int. J. Adv. Manuf. Technol.* **2016**, *86*, 3483–3494. [\[CrossRef\]](#)
- Özcan, M.; Vallittu, P.K. Effect of surface conditioning methods on the bond strength of luting cement to ceramics. *Dent. Mater.* **2003**, *19*, 725–731. [\[CrossRef\]](#)
- Shen, X.; Zhang, J.; Xing, D.; Zhao, Y. A study of surface roughness variation in ultrasonic vibration-assisted milling. *Int. J. Adv. Manuf. Technol.* **2012**, *58*, 553–561. [\[CrossRef\]](#)
- Zahedi, A.; Tawakoli, T.; Akbari, J. Energy aspects and workpiece surface characteristics in ultrasonic-assisted cylindrical grinding of alumina–zirconia ceramics. *Int. J. Mach. Tools Manuf.* **2015**, *90*, 16–28. [\[CrossRef\]](#)
- Dong, S.; Zheng, K.; Xiao, X. Ultrasonic vibration assisted grinding of sintered dental zirconia ceramics: An experimental study on surface roughness. *Int. Adv. Mater. Res.* **2014**, *1017*, 800–805. [\[CrossRef\]](#)
- Park, K.H.; Hong, Y.H.; Kim, K.T.; Lee, S.W.; Choi, Y.J. Understanding of ultrasonic assisted machining with diamond grinding tool. *Mod. Mech. Eng.* **2014**, *4*, 1–7. [\[CrossRef\]](#)
- Ghazal, M.; Yang, B.; Ludwig, K.; Kern, M. Two-body wear of resin and ceramic denture teeth in comparison to human enamel. *Dent. Mater.* **2008**, *24*, 502–507. [\[CrossRef\]](#)
- Chen, H.; Tang, J. A model for prediction of surface roughness in ultrasonic-assisted grinding. *Int. J. Adv. Manuf. Technol.* **2015**, *77*, 643–651. [\[CrossRef\]](#)
- Zhang, J.; Wang, L.; Tian, F.; Yan, Z.; Zhi, W. Modeling study on surface roughness of ultrasonic-assisted micro end grinding of silica glass. *Int. J. Adv. Manuf. Technol.* **2016**, *86*, 407–418. [\[CrossRef\]](#)
- Wu, C.; Li, B.; Liu, Y.; Liang, S.Y. Surface roughness modeling for grinding of Silicon Carbide ceramics considering co-existence of brittleness and ductility. *Int. J. Mech. Sci.* **2017**, *133*, 167–177. [\[CrossRef\]](#)
- Wu, J.; Cheng, J.; Gao, C.; Yu, T.; Guo, Z. Research on predicting model of surface roughness in small-scale grinding of brittle materials considering grinding tool topography. *Int. J. Mech. Sci.* **2020**, *166*, 105263. [\[CrossRef\]](#)
- Agarwal, S.; Rao, P.V. Modeling and prediction of surface roughness in ceramic grinding. *Int. J. Mach. Tools Manuf.* **2010**, *50*, 1065–1076. [\[CrossRef\]](#)
- Bi, Z.; Tokura, H.; Yoshikawa, M. Study on surface cracking of alumina scratched by single-point diamonds. *J. Mater. Sci.* **1988**, *23*, 3214–3224. [\[CrossRef\]](#)
- Liu, D.; Cong, W.L.; Pei, Z.J.; Tang, Y. A cutting force model for rotary ultrasonic machining of brittle materials. *Int. J. Mach. Tools Manuf.* **2012**, *52*, 77–84. [\[CrossRef\]](#)
- Zhang, C.; Zhang, J.; Feng, P. Mathematical model for cutting force in rotary ultrasonic face milling of brittle materials. *Int. J. Adv. Manuf. Technol.* **2013**, *69*, 161–170. [\[CrossRef\]](#)
- Marshall, D.B.; Lawn, B.R.; Evans, A.G. Elastic/plastic indentation damage in ceramics: The lateral crack system. *J. Am. Ceram. Soc.* **1982**, *65*, 561–566. [\[CrossRef\]](#)
- Jiao, F. The Theoretical and Experimental Studies on Ultrasonic Aided High Efficiency Lapping with Solid Abrasive of Engineering Ceramic. Ph. D. Thesis, Shanghai Jiao Tong University, Shanghai, China, 2008.

21. Pei, Z.J.; Ferreira, P.M.; Kapoor, S.G.; Haselkorn, M. Rotary ultrasonic machining for face milling of ceramics. *Int. J. Mach. Tools Manuf.* **1995**, *35*, 1033–1046. [[CrossRef](#)]
22. Agarwal, S.; Rao, P.V. A probabilistic approach to predict surface roughness in ceramic grinding. *Int. J. Mach. Tools Manuf.* **2005**, *45*, 609–616. [[CrossRef](#)]
23. Younis, M.A.; Alawi, H. Probabilistic analysis of the surface grinding process. *Trans. Can. Soc. Mech. Eng.* **1984**, *8*, 208–213. [[CrossRef](#)]
24. Ding, K.; Fu, Y.; Su, H.; Gong, X.; Wu, K. Wear of diamond grinding wheel in ultrasonic vibration-assisted grinding of silicon carbide. *Int. J. Adv. Manuf. Technol.* **2014**, *71*, 1929–1938. [[CrossRef](#)]